Polar Kerr effect studies of $Ga_{1-x}Mn_xAs$ epitaxial films

R. Lang, A. Winter, and H. Pascher*
Experimentalphysik I, Universitt Bayreuth, D-95440 Bayreuth, Germany

H. Krenn
Institut fr Experimentalphysik, Karl-Franzens-Universitt Graz, A-8010 Graz, Austria

X. Liu and J. K. Furdyna
Department of Physics, University of Notre Dame, Notre Dame, Indiana 46556, USA
(Received 2 February 2005; revised manuscript received 25 May 2005; published 14 July 2005)

The ferromagnetic state of thin $Ga_{1-x}Mn_xAs$ layers ($d=300$ nm; $x=0.014$, $p=6.7\times10^{19}$ cm^{-3}, $T_C=40$ K, easy axis in plane; $x=0.03$, $p=9.5\times10^{18}$ cm^{-3}, $T_C=60$ K, easy axis out of plane) on GaAs substrates is investigated by polar magneto-optical Kerr effect (MOKE) and reflectance magnetocircular dichroism (MCD) studies in the temperature range between 1.6 K and 100 K, in magnetic fields normal to the layer plane ranging from −5 to +5 kOe. A magnetic field of 70 kOe is applied in those cases when truly saturated magnetization has to be determined. A parabolic interband dielectric function model that includes the relevant (heavy-hole, light-hole, and split-off) valence bands, as well as the finite Moss-Burstein shift, was developed for analyzing both the MOKE and MCD. The occupation of the spin-split valence bands is taken into account by explicitly including the Fermi level for holes in analytic form. The samples were sufficiently different in their Curie temperatures, easy axis directions, magnetic ion contents, and hole concentrations to demonstrate experimentally the versatility of the proposed model. Superconducting quantum interference device measurements carried out on the samples demonstrated the validity of the dilute-magnetic-semiconductor (DMS) mean-field approach for the contact exchange interaction between manganese spins and hole carriers, reflected by a more or less *fixed* conduction-band exchange parameter $N_0\alpha=0.22-0.29$ eV and a hole exchange parameter $N_0\beta$ varying between 0.9 and 2.3 eV, depending on the hole concentration and on the Mn content. Note that the magnitudes are close to those familiar from II-VI DMS's, but the sign of $N_0\beta$ is reversed from the II-VI case—i.e., from antiferromagnetic to ferromagnetic local exchange. The quantitative wavelength-dependent ($\lambda=550-950$ nm) analysis of MOKE and MCD spectra for both samples and the imposed requirement that the band parameters should not deviate significantly from the GaAs-related band alignment and from exchange-induced spin multiplicities lead us to the introduction of a dispersionless level superimposed in the conduction band of GaMnAs (fitted energy gaps 1.50–1.57 eV). The physical nature of such a level could not be identified by our simplified model, but we note that a high-density-of-states level in the conduction band of GaMnAs has been predicted recently by Sandratskii and Bruno [Phys. Rev. B **66**, 134435 (2002)]. The hysteresis measurements are presented without deeper analysis. The hole concentration fitted to MOKE and MCD spectra deviates for the $x=0.014$ sample by a factor of 0.8 from the data obtained by anomalous Hall effect measurements, but this inconsistency should probably be viewed as a result of the difficulty in interpreting experimental magnetotransport measurements, rather than a shortcoming of our theoretical treatment.

DOI: 10.1103/PhysRevB.72.024430 PACS number(s): 75.50.Pp, 75.60.−d, 78.66.Fd

I. INTRODUCTION

The discovery of high-temperature ferromagnetism ($T_c=110$ K) in the dilute magnetic semiconductor (DMS) GaMnAs (Ref. 1) has promoted very intense research on the exchange interaction mechanisms in III-V semiconductors alloyed with magnetic ions. The long-range parallel alignment of Mn spins accompanied by spin-polarized energy bands opens new ways of controlling both magnetic and semiconductor properties by changing the carrier characteristics, such as concentration and spin alignment. In contrast to ferromagnetic metals, DMS ferromagnets are efficient spin injectors across magnetic and nonmagnetic heterojunctions, and GaMnAs/AlAs/GaMnAs single-barrier tunnel junctions have already been shown to exhibit large tunneling magnetoresistance (maximum 75%) at 8 K.[2]

The study of magnetic properties of GaMnAs and related III-Mn-V ferromagnetic semiconductors is commonly accomplished by superconducting quantum interference device (SQUID) magnetometry as well as by magneto-optical Faraday and Kerr effect measurements. The magnetization reversal process and the domain wall motion, as well as domain rotation, have been investigated experimentally by Shono *et al.*[3] and theoretically by Dietl *et al.*[4] Polar, longitudinal, and transverse Kerr rotation in GaMnAs layers, applying a magnetic field along different crystal directions, has been studied by Hrabovsky *et al.*[5] A blueshift of magneto-optical spectra due to quantum confinement and ferromagnetism has been observed by Shimizu and Tanaka even in ultrathin (<5 nm) ferromagnetic GaMnAs/AlAs superlattices (see Ref. 6), and the spin dynamics in epitaxial films

and in AlAs/GaMnAs/AlAs single quantum wells have been measured by time-resolved Kerr rotation.[7,8]

The physics of hysteresis effects in ferromagnetic GaMnAs is still under debate. Magnetic anisotropy and magnetization reversal phenomena have been studied by Moore *et al.*[9] using Kerr rotation and magnetic linear dichroism. Magnetic anisotropy depends on the hole concentration in the spin-split valence band and on the local site disorder of Mn atoms.[10,11] In GaMnAs epilayers the biaxial strain influences the direction of the easy axis of magnetization: Compressive strain of a GaMnAs layer on GaAs substrate prefers an in-plane magnetization, whereas tensile strain of a GaMnAs layer on (In,Ga)As buffer layers causes the easy axis to lie perpendicular to the film plane. However, this rule of thumb may be relaxed for certain Mn and hole concentrations, and could depend on the fabrication procedure, the layer thicknesses, and even on the temperature range.[12]

The magneto-optical spectra of GaMnAs outline different absorption edges for the two circular photon polarizations (σ^+, σ^-). Interestingly, these occur in opposite order compared to II-VI DMS's like CdMnTe. It has been shown that this order reversal of absorption edges results from the Moss-Burstein shift—that is, from the shifts of the absorption edges associated with the unfilled portions of the valence subbands in *p*-type GaMnAs.[13] In earlier studies the Moss-Burstein shift has been taken into account by adjusting the proper band gap (E_g) in the absorption model of magnetocircular dichroism (MCD), which differed significantly from the energy gap of GaAs (despite the rather low Mn content $x<0.05$). For a quantitative and consistent analysis of Kerr rotation and MCD spectra this heuristic accommodation of an energy gap is not satisfactory, and it does not quantitatively reconcile the experimental spectra—a handicap that continues to be present in the evaluation of magneto-optical data observed on these alloys. The contribution of hole spin polarization to the magneto-optic spectra is still not well understood and may lead to differences with SQUID magnetization data—a matter that has been addressed by Beschoten *et al.*[14]

In this work we derive a dielectric function for GaMnAs, including the spin splitting of valence bands as it is established in mean-field DMS exchange interaction models in combination with the Kohn-Luttinger Hamiltonian (see Ref. 10). Fitting this model to our experimental findings enforces a reversal of the sign of the splitting of heavy- and light-hole valence bands in GaMnAs, as compared to the values familiar from II-VI DMS's apparently induced by strong hybridization of spin-polarized holes with Mn *d* levels. This leads to strong kinetic exchange coupling between hole spins and Mn spins. In our analysis we start from the bare (parabolic) band structure of GaAs; i.e., the band-edge parameters should not deviate much from GaAs parameters for a wide range of carrier concentrations. Particularly, a parabolic valence-band dispersion is anticipated, and the Moss-Burstein shift is taken into account for an approximately fixed energy gap (E_g), using a corresponding Fermi energy level in the highest split valence band as an explicit parameter. To achieve even a first-order agreement of the model with measured Kerr rotation and MCD over a broad spectral range from 500 nm to 1000 nm we fitted the "bare" GaMnAs band gap (without exchange splitting), the *p-d* exchange parameters, and the hole concentration correspondingly. To our knowledge this is the first model calculation of the Kramers-Kronig-compatible dielectric function, derived for GaMnAs over a range of moderate hole concentrations ($5\times10^{18}\ \mathrm{cm}^{-3} \leqslant p \leqslant 1\times10^{20}\ \mathrm{cm}^{-3}$). In order to avoid complications arising from the ferromagnetic domain structure, the samples were exposed to a strong magnetic field to ensure a uniform perpendicular magnetization.

We investigated thin layers (300 nm) of $Ga_{1-x}Mn_xAs$ with sufficiently different x content (0.014 and 0.03) and moderate hole concentrations ($6.7\times10^{19}\ \mathrm{cm}^{-3}, 9.5\times10^{18}\ \mathrm{cm}^{-3}$). The corresponding Curie temperatures are 40 K and 60 K, respectively. We compare magnetization data obtained by SQUID magnetometry with Kerr and MCD reflectivity under various magnetic fields and temperatures. Experimental details, including sample characteristics, are presented in Sec. II. In Sec. III we present a comprehensive theory of an interband dielectric function for $Ga_{1-x}Mn_xAs$ and its relation to the Kerr effect and MCD. It is emphasized particularly that MCD and Kerr data are explained in terms of the same model, with the same set of parameters. In Sec. IV the magnetic field, temperature, and wavelength dependences of the measured SQUID, Kerr rotation, and MCD data are discussed and compared with theory.

II. EXPERIMENTAL METHOD AND INVESTIGATED MATERIALS

A. GaMnAs samples

The equilibrium solubility of Mn in GaAs is known to be at most $10^{19}\ \mathrm{cm}^{-3}$. At higher Mn concentrations in materials grown under equilibrium conditions, the formation of MnAs clusters within the GaAs host material is observed. Nonequilibrium growth techniques, however, such as low-temperature molecular beam epitaxy (LT-MBE), allow one to obtain homogeneous alloys with Mn concentrations up to nearly 10%.

The alloy system $Ga_{1-x}Mn_xAs$ becomes ferromagnetic for $x>0.01$.[15] A phase diagram has been published by Oiwa *et al.*[16]

If the epitaxial films are grown on (100) GaAs, the strain via the magnetoelastic interaction enforces the easy axis of magnetization to lie in the layer plane. If an InGaAs buffer is grown between substrate and $Ga_{1-x}Mn_xAs$ with sufficient In content, the tensile strain causes the easy axis to lie perpendicular to the film surface—i.e., along the [100] direction.[17]

The experiments reported here were carried out on two epitaxial GaMnAs films with 1.4% and 3.0% Mn, respectively, both 300 nm thick. In the case of the 1.4% Mn sample first a GaAs buffer layer was grown on a semi-insulating (100) GaAs substrate under standard growth conditions (590 °C). After that the substrate temperature T_s was reduced to 200–300 °C and a 100-nm LT GaAs buffer layer was deposited. The $Ga_{1-x}Mn_xAs$ was then grown at the rate of about 0.8 μm/h.

In the case of the 3% Mn sample, an additional GaInAs layer with 20% In and a thickness of 1000 nm was grown on

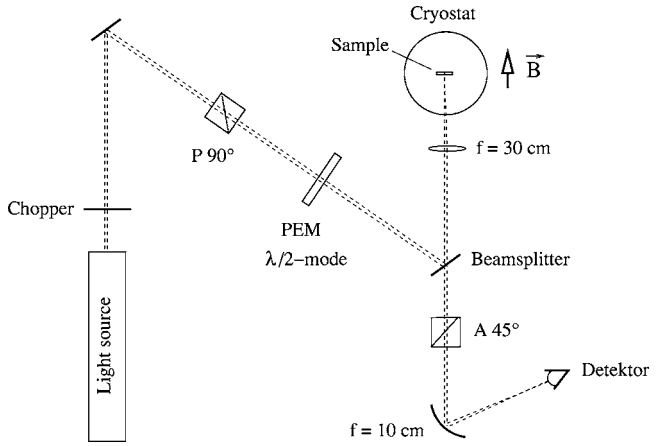

FIG. 1. Schematic sketch of the experimental setup. The principle of operation is explained in the text.

the LT-GaAs buffer before the deposition of the 300-nm-thick $Ga_{0.97}Mn_{0.03}As$ layer. As noted above, the additional InGaAs layer forces the easy axis of magnetization of the GaMnAs film to lie in a direction perpendicular to the film, whereas the easy axis of the sample with 1.4% Mn grown directly on the LT GaAs buffer lies in the layer plane.

Reflection high-energy electron diffraction (RHEED) was used to monitor the surface reconstruction during the growth, which was always carried out under As-stabilized conditions. Since the lattice constant of zinc-blende GaMnAs increases with the Mn concentration x, this provided the opportunity to determine the Mn concentration x using x-ray diffraction (XRD) as discussed in Refs. 18 and 19.

The experimental determination of the hole concentration by room-temperature Hall effect measurements has yielded $p=8.7\times10^{19}$ cm^{-3} for the $x=0.014$ sample and $p=7.6\times10^{18}$ cm^{-3} for $x=0.03$. While Hall measurements on GaMnAs are affected by complications arising from the anomalous Hall effect (AHE), in the case of room-temperature measurements on samples with low Mn and carrier concentrations these complications have been shown to be small and thus provide a useful estimate of p.[20] Note that these values of p are in reasonable agreement with the hole concentrations obtained from fits to the Kerr and MCD data ($p=6.7\times10^{19}$ cm^{-3} for $x=0.014$ and $p=9.5\times10^{18}$ cm^{-3} for $x=0.03$) mentioned earlier.

B. Experimental setup

Figure 1 shows a schematic diagram of the experimental setup used for the polar Kerr effect measurements. A halogen lamp, a grating spectrometer, and a Ti:sapphire laser, as well as laser diodes operating at various wavelengths, were used as light sources.

Behind the first polarizer P90° the light is polarized vertically. After passing the photoelastic modulator (PEM) the polarization vector of the light is switched from vertical to horizontal polarization with a frequency of ~50 kHz. The light reflected from the sample is detected after passing through the analyzer A45°, oriented 45° off the vertical direction.

At $B=0$ the projections of the electric field orientations behind the PEM on the direction of the analyzer are equal. A lock-in amplifier that obtains its reference from the modulator and the signal from the detector measures the difference between the two projections (which at $B=0$ is zero).

If the sample rotates the plane of polarization, the difference between the two projections no longer vanishes and is detected by the lock-in amplifier. We refer to this signal as "DLI." A second lock-in, amplifier receiving its reference from the chopper, measures the overall intensity "SLI." From both signals the rotation angle ψ of the polarization of the reflected light can be calculated from

$$\psi=\frac{1}{2}\arcsin\frac{\frac{DLI}{SLI}}{\frac{I_2}{8}-\frac{I_1}{2\pi}\frac{DLI}{SLI}}. \tag{1}$$

The constants I_1 and I_2 can be calculated numerically on the basis of the working principle of a lock-in amplifier. However, even small misalignments of the directions of the polarizers affect these constants. Therefore, in order to improve experimental accuracy, the constants were determined from a calibration experiment using the Faraday rotation of a paramagnetic $Cd_{0.9}Mn_{0.1}Te$ sample. This sample also serves as an immediate reference check for the correct sign of Kerr rotation of GaMnAs samples; see Fig. 7 below.

The use of a differential method makes this experimental setup highly sensitive, enabling us to resolve rotations of the polarization of the reflected light with an accuracy of up to 0.002 degree. This value is estimated from the signal-to-noise ratio of the measurement shown in Fig. 2(a).

Since the samples are located inside a cryostat, the incident as well as the reflected light has to pass two cryostat windows, which rotate the polarization of the light due to the Faraday effect of the window material. This rotation angle has to be subtracted from each measurement to get the Kerr rotation of the sample itself.

For the measurement of MCD, the PEM is used in the $\lambda/4$ mode and the analyzer behind the sample is removed. Then the DLI lock-in amplifier measures the difference of the reflected intensities R^+ and R^- of the σ^+ and σ^- polarizations, and the SLI lock-in amplifier measures their sum. From both quantities the values of R^+ and R^- can then be readily obtained.

C. Magnetic field and temperature dependence of the Kerr rotation

Typical magneto-optical Kerr effect (MOKE) measurements are shown in Fig. 2. Figure 2(a) corresponds to the GaMnAs sample with 1.4% Mn, which has the easy axis in the layer plane—i.e., perpendicular to $\vec{B}$. Figure 2(b) is for the sample with 3.0% Mn (easy axis perpendicular to film plane). The arrows indicate the sweep direction of the magnetic field. Figure 2(b) shows an usual hysteresis loop centered at $B=0$. The coercive field is 122 Oe. Saturation magnetization (M_s) in Fig. 2(b) corresponds to the rotation of 0.175°. The inset shows a comparison between SQUID mag-

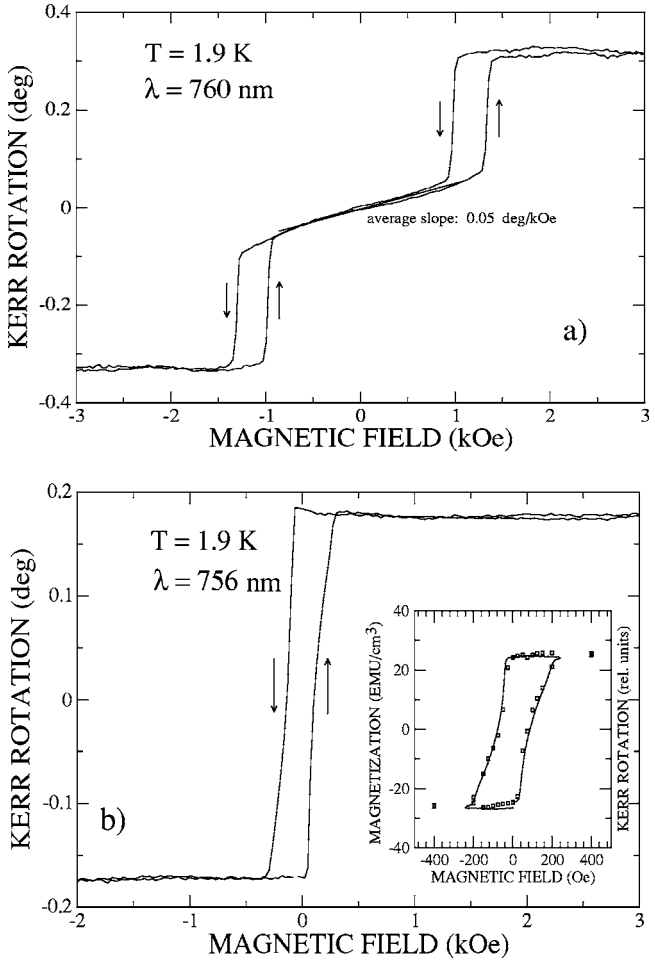

FIG. 2. Kerr rotation angle as a function of magnetic field. Note the slope of the curve between the two hysteresis loops in (a). (a) Sample with easy axis in the layer plane, Mn content 1.4%; (b) sample with easy axis perpendicular to the layer plane, Mn content 3%. Inset in (b): Squares: magnetization (left-hand ordinate) vs magnetic field. Solid curve: Kerr angle (right-hand ordinate) vs magnetic field.

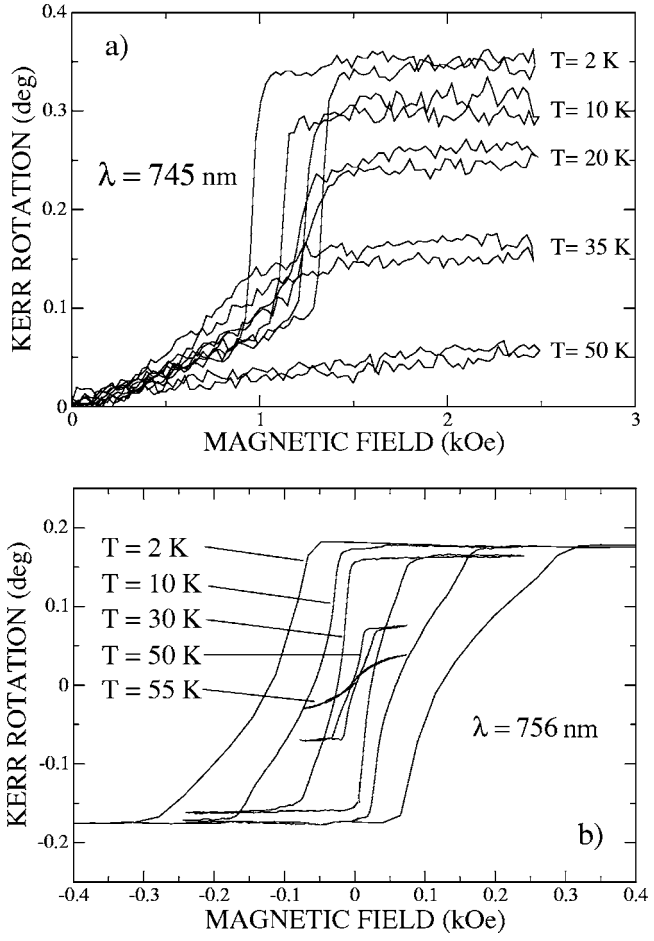

FIG. 3. Kerr rotation angle as a function of magnetic field at various temperatures. (a) Sample with easy axis in the layer plane, Mn content 1.4%; (b) sample with easy axis perpendicular to the layer plane, Mn content 3%.

netization data (squares) and Kerr rotation (solid curve). The SQUID data were taken at $T=5$ K. The measured value $M_s=24.3$ emu/cm^3 corresponds to a Kerr rotation of 0.175°.

The trace in Fig. 2(a) exhibits a rather unexpected behavior. It shows two hysteresis loops symmetrically with respect to $B=0$. At $B=0$ the magnetization is aligned in plane due to the combined effects of shape, cubic (K_1), and uniaxial anisotropy (K_2).[21] The occurrence of the shifted hysteresis requires these additional anisotropy terms, since without them the snap-out of the magnetization at finite magnetic field cannot be described. This strange behavior occurs when the sample layer is characterized by distinct in-plane easy axes ([001],[011]) and the magnetization vector is tilted out of the layer plane by the field normal to the layer.[9] As seen in Fig. 2(a), the Kerr rotation at low fields increases linearly with the field without any hysteresis splitting, indicating a gradual tilting of the magnetization by an angle ϑ from the film plane. At the threshold field $B_{th}=0.13$ T the magnetization "snaps" out from the nearly coplanar to the perpendicular direction ($\vartheta_{min}=90°$), providing full saturation perpendicular to the layer. For this value of B_{th} and after minimizing the total anisotropy energy, we obtain $K_1=3.1\times10^3$ J/m^3 if we assume the value of $M_s=13.3$ emu/cm^3 for the saturation magnetization and neglect K_2. This positive value of K_1 agrees with data from literature:[10] 2–4 kJ/m^3.

In Fig. 3 the Kerr rotation angle for the two samples is shown for five temperatures. From Fig. 3(a), corresponding to the sample with the easy axis in the layer plane, one can see that the slope of the Kerr rotation angle slightly increases for increasing temperatures below T_c. This indicates a reduction of the anisotropy constant K_1 with T. Above the Curie temperature the spontaneous magnetization vanishes, and the corresponding rather flat magnetization curves correspond to a weak Brillouin-type (hysteresis-less) paramagnetic behavior. For $T<T_c$ one can notice an increase of the saturation magnetization, as well as a strengthening of the magnetocrystalline anisotropy, as is reflected by the wider opening of hysteresis loops (implying an increasing coercive field).

The temperature dependences of the Kerr rotation corresponding to saturation magnetization and widths of the hysteresis loops for the two samples are shown in Figs. 4 and 5, respectively. The abscissas are normalized to the respective Curie temperatures T_c—i.e., 40 K for the sample with 1.4%

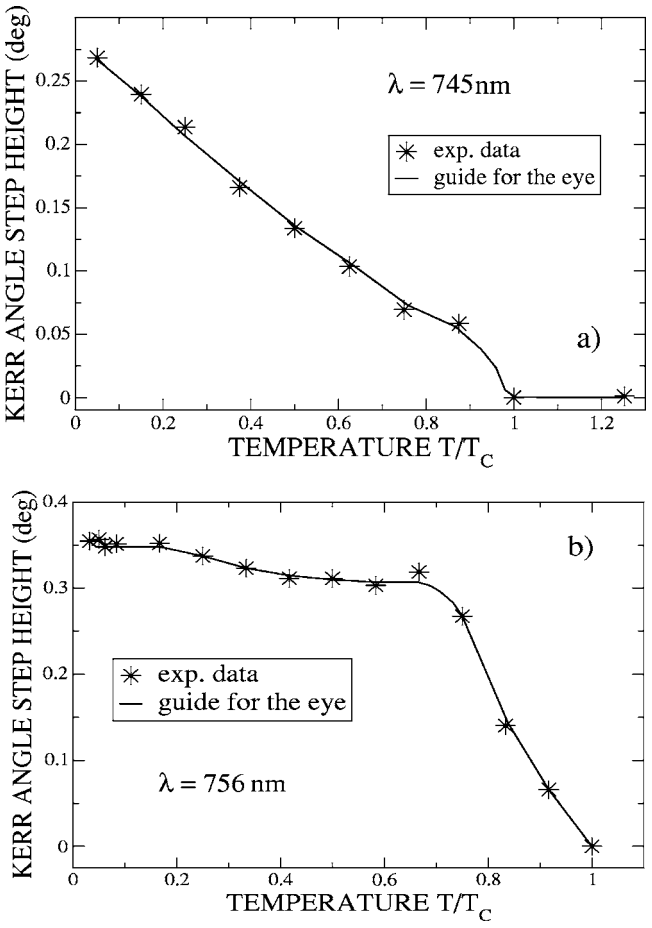

FIG. 4. Kerr rotation corresponding to magnetization saturated perpendicular to the layer plane as a function of temperature. (a) Sample with easy axis in the layer plane, Mn content 1.4%; (b) sample with easy axis perpendicular to the layer plane, Mn content 3%.

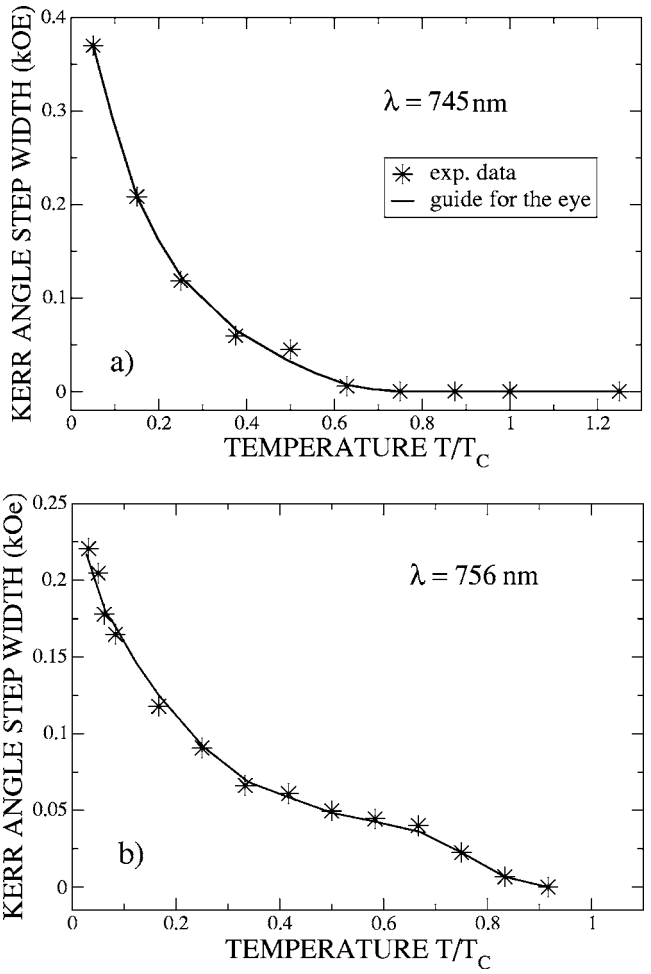

FIG. 5. Width of the hysteresis loops as a function of temperature. (a) Sample with easy axis in the layer plane, Mn content 1.4%; (b) sample with easy axis perpendicular to plane, Mn content 3%.

Mn [Figs. 4(a) and 5(a)] and 60 K for the sample with 3% Mn [Figs. 4(b) and 5(b)]. As mentioned above the temperature dependence of the measured values for H beyond the hysteresis loops reflects M_s(T). Figure 4(a) shows an approximately linear behavior, which is unusual for a ferromagnet. Recent calculations on this subject are presented by Das Sarma *et al.*[22]

The dependences measured for the 3% sample (easy axis perpendicular to the film) exhibit kinks at $\sim 0.65T_c$ [see Figs. 4(b) and 5(b)]. This indicates a change in the physical properties of the sample at this temperature. We expect that this is due to a change of the magnetic anisotropy that switches from an out-of-plane easy direction (at $T<\frac{2}{3}T_c$) to an in-plane anisotropy (at $T>\frac{2}{3}T_c$), similar to that observed by direct magnetization measurements for GaMnAs specimens with comparable Mn and hole concentrations.[23] Since our samples exhibit various magnetic easy and hard axes and a strongly temperature-dependent magnetization [see, e.g., Fig. 4(a)], the wavelength dependence of Kerr rotation and MCD were measured at $T=1.8$ K ($\ll T_c$) to ensure homogeneous saturation of the magnetization perpendicular to the layer. These spectral data will be presented and discussed in Sec. IV after we present the theoretical model in Sec. III.

III. THEORY OF INTERBAND POLAR KERR ROTATION AND MAGNETOCIRCULAR DICHROISM IN HEAVILY DOPED GaMnAs

In this section we adopt a parabolic band model as in Ref. 24, and we calculate the interband dielectric function after introducing the exchange spin splitting in mean-field and virtual-crystal approximations, taking the Moss-Burstein effect explicitly into account.

In a somewhat different approach (in order to allow for multiple reflection interferences) the amplitude of the reflection coefficients for left- and right-circularly polarized light in a thin sample is calculated and these (complex) reflection coefficients are related to the wavelength-dependent Kerr rotation angle and MCD. Interband transitions to the conduction band from the partly populated heavy- and light-hole valence bands and the fully occupied split-off valence band are calculated. In order to restrict the parameters for the complex dielectric function to those which are physically relevant, it is assumed that the samples are exposed to a saturating perpendicular magnetic field (>1 T) and to very low temperatures ($1.8\ \text{K} \ll T_c$). Thus the magnetic ions are fully aligned perpendicularly to the film plane, and thermal fluc-

tuations deviating from the magnetic ground state can be neglected. The intraband free-carrier absorption of the holes in *p*-GaMnAs can be neglected for photon energies >1.5 eV, although their population influence (i.e., the Moss-Burstein shift) on the interband transitions has to be implicitly taken into account for the calculation of the interband dielectric function.

We augment the derivation of optical dispersion relations given in Ref. 24 for E_0 and $E_0+\Delta_0$ transitions in the limit of parabolic bands by explicitly implementing the Moss-Burstein shift in the Kramers-Kronig pairs of the dielectric function. The absorption part $[\varepsilon_2(\omega)]$ is constructed to give δ-like (momentum conserving) transitions, neglecting any level broadening due to damping. By this means it is possible to formulate an analytic Kramers-Kronig (KK) transformation even for finite Fermi energy in a parabolic band (the details are treated in the Appendix). After implementing the KK transformation, a level broadening is introduced, via a damping parameter Γ, by generalizing the photon energy $\hbar\omega \Rightarrow \hbar\omega + i\hbar\Gamma$. It is expected that damping will be particularly important for the strong exchange scattering of holes with randomly distributed magnetic (Mn^{2+}) ions.

In order to adopt a scale, we take the zero-energy reference point at the top of the heavy-hole band. Hence the conduction-band edge is located at E_g, and the hole Fermi energy at $-E_F$. The interband absorption thus sets in at $\hbar\omega = E_g + E_F$, where $\hbar\omega$ is the photon energy. The ω-dependent dielectric function is given by (see the Appendix)

$$\begin{aligned}\varepsilon(\omega) = \varepsilon_\infty &+ 2f\frac{\sqrt{E_g}}{(\hbar\omega)^2}\left[1 - \frac{2}{\pi}\arctan\sqrt{\frac{E_F}{E_g}}\right] \\ &- f\frac{\sqrt{E_g}}{(\hbar\omega)^2}\sqrt{1+\frac{\hbar\omega}{E_g}}\left[1 - \frac{2}{\pi}\arctan\sqrt{\frac{E_F}{E_g+\hbar\omega}}\right] \\ &- f\frac{\sqrt{E_g}}{(\hbar\omega)^2}\sqrt{1-\frac{\hbar\omega}{E_g}}\left[1 - \frac{2}{\pi}\arctan\sqrt{\frac{E_F}{E_g-\hbar\omega}}\right].\end{aligned} \tag{2}$$

Equation (2) is an extension of the original expression given in Ref. 24, taking into account a nonzero Fermi energy E_F in the heavy-hole (HH) band. f is the electric-dipole oscillator strength for the HH to conduction (C) band transition. The real function $\varepsilon(\omega)$ can be analytically extended to the complex ω plane by introducing the damping parameter Γ through the transformation

$$\omega \rightarrow \omega + i\Gamma. \tag{3}$$

Hence, $\varepsilon(\omega)$ represents the correct causal dielectric function consisting of KK-related real and imaginary parts. In a ferromagnetic semiconductor the bands are spin split [see Eqs. (6)–(8) below] due to the symmetry breaking by the spontaneous field- and temperature-dependent magnetization $M(T,H)$ of the material. This splitting can be implemented in the $\vec{k}\cdot\vec{p}$ perturbation theory according to the conventional six-band Luttinger-Kohn Hamiltonian scheme[10] and expressed in terms of the Kondo exchange interaction constants $J_{s,p\text{-}d}$:

$$\Delta_{s,p\text{-}d}(H,T) = A_F J_{s,p\text{-}d}\frac{M(H,T)}{g\mu_B}. \tag{4}$$

The Mn spins in $Ga_{1-x}Mn_xAs$ are assumed to be in the d^5 configuration, so that at $T \ll T_c$ in a saturating field $\langle S_z\rangle = S = \frac{5}{2}$ and the Landé factor $g=2$. The magnetization of the sample is expressed by microscopic parameters, like the thermal average of a single Mn spin $\langle S_z\rangle$, as

$$M(H,T) = g\mu_B x\langle S_z\rangle_{H,T} N_0. \tag{5}$$

For the conduction electron (s-d) exchange energy we adopt approximately the same value as for II-VI DMS's: $J_{sd} = \alpha = 0.01-0.013$ eV nm^3, corresponding to $\alpha N_0 = 0.22-0.29$ eV, $N_0 = 2.21\times 10^{22}$ cm^{-3} being the cation concentration of the GaAs host crystal. For the hole (p-d) exchange interaction, different values are given in the literature, ranging from $J_{pd} = -\beta = 0.054$ eV nm^{-3} to 0.1 eV nm^{-3} corresponding to βN_0 from -1.2 eV to -2.2 eV, respectively. A_F in Eq. (4) is the Fermi liquid parameter and equals 1.2 for the carriers in the valence band which form a correlated hole liquid. The individual exchange splittings of the various bands participating in the σ^+ and σ^- interband transitions are the following.

Conduction band $|c\rangle = |\mathrm{CB}, j\rangle$:

$$\Delta_c(j) = j\cdot 2J_{sd}\frac{M(H,T)}{g\mu_B} = j\cdot x\langle S_z\rangle 2N_0\alpha \quad \left(j = \pm\frac{1}{2}\right). \tag{6}$$

Valence bands $|v\rangle = |\mathrm{HH}, \mathrm{LH}, j\rangle$:

$$\begin{aligned}\Delta_v(j) &= j\cdot A_F\frac{2}{3}J_{pd}\frac{M(H,T)}{g\mu_B} \\ &= j\cdot A_F x\langle S_z\rangle\frac{2}{3}N_0\beta \quad \left(j = -\frac{3}{2},\ldots,+\frac{3}{2}\right).\end{aligned} \tag{7}$$

Split-off band $|\mathrm{SO}, j\rangle$:

$$\Delta_{so}(j) = j\cdot A_F\frac{2}{3}J_{pd}\frac{M(H,T)}{g\mu_B} = j\cdot A_F x\langle S_z\rangle\frac{2}{3}N_0\beta \quad \left(j = \pm\frac{1}{2}\right). \tag{8}$$

The sign convention in Eqs. (6)–(8) is according to the commonly accepted DMS picture: For antiferromagnetic exchange $N_0\beta < 0$, as in II-VI-based DMS's, the top heavy-hole valence-band level possesses the angular momentum $j = -3/2$. As will be seen by inspection of Fig. 7, this spin ordering is reversed in GaMnAs (if $N_0\beta > 0$), a feature that is already seen even in paramagnetic GaMnAs ($x=0.005$).

These spin splittings of the respective bands reflect the thermodynamic magnetization, as measured by magnetometry. Whether magneto-optic experiments such as the Kerr effect actually correspond to the thermodynamic magnetization is questionable, particularly for ferromagnetic semiconductors with strong spin polarization of the carriers themselves. Magneto-optical experiments deviating from thermodynamic magnetization have been reported in the literature.[14] It is therefore important to compare Kerr mea-

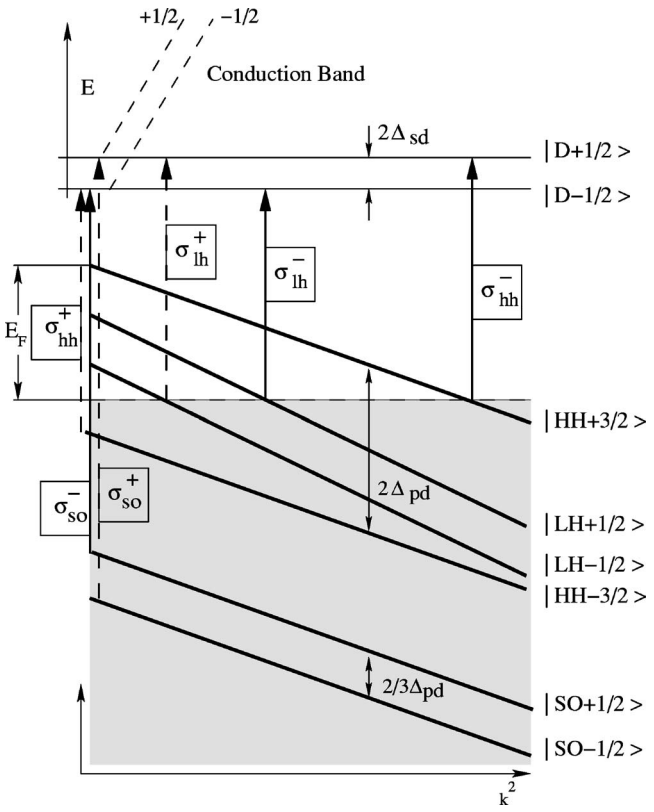

FIG. 6. Typical energy level scheme for a saturated ferromagnetic $Ga_{1-x}Mn_xAs$ sample ($x=0.014, p=8\times10^{19}$ cm^{-3}). Solid arrows: left-hand circularly polarized interband transition ($\sigma^-;\Delta j=-1$); dashed arrows: right-hand circularly polarized interband transition ($\sigma^+;\Delta j=+1$).

surements with results from magnetization studies using SQUID magnetometry [see Fig. 2(b) and corresponding discussion].

A typical level scheme for a saturated ferromagnetic $Ga_{1-x}Mn_xAs$ sample ($x=0.014, p=8\times10^{19}$ cm^{-3}), showing the allowed circularly polarized (σ^+,σ^-) interband transitions, is plotted in Fig. 6. The solid and dashed arrows represent the left- and right-handed circularly polarized transitions ($\Delta j=-1$) and ($\Delta j=+1$), respectively.

Note that the heavy-hole and light-hole bands are labeled in terms of hole spin quantum numbers (j) in reverse order, opposite to the scheme used for II-VI DMS's. This can be shown experimentally by comparing the Faraday rotation in dilute magnetic CdMnTe ($x=0.10$) and in paramagnetic GaMnAs ($x=0.005$). From Fig. 7 it is seen that the slopes are opposite in sign, clearly demonstrating the difference in the exchange coupling in II-VI and III-V DMS's. Anticipating the remarks in the Conclusion (Sec. V), we note also at this point that our Kerr rotation and MCD measurements can only be *quantitatively* explained if the terminating level in the participating interband transitions is not the highly dispersive conduction band, but rather a dispersionless level $|D,j\rangle$ attached to the Mn site (and correspondingly spin split).

We measure the Fermi level from the top of the uppermost spin-split heavy-hole band $|\mathrm{HH},+3/2\rangle$, and we take

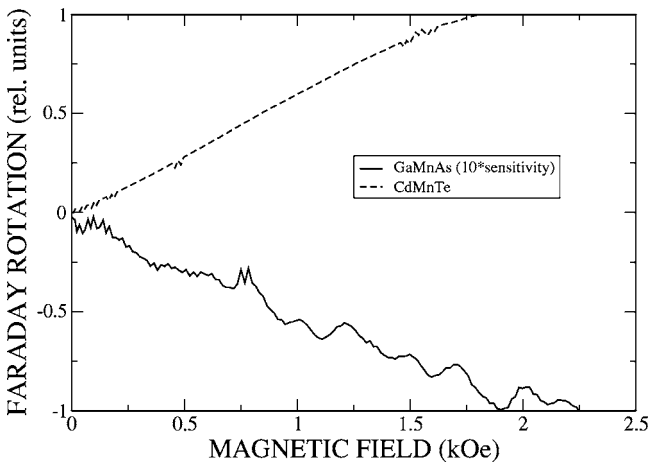

FIG. 7. Comparison of the sign of Faraday rotation in CdMnTe (Mn content: 10%) and paramagnetic GaMnAs (Mn content: 0.5%), $\lambda=1060$ nm, $T=1.8$ K.

into account the corresponding Moss-Burstein shifts for each valence band in order to find out the onset of the corresponding interband transitions. We treat the interband magnetooptical Kerr effect by considering all the spin splittings—the one of the HH and D levels, the splittings of the light-hole (LH) band, and finally the contribution of the split-off (SO) band. The spin splitting is dominated by the (ferromagnetic, $\beta N_0>0$) heavy-hole exchange interaction. Through this interaction the semiconductor gap (E_g) is opened wider for the σ^+ interband transitions than for the σ^- interband transitions, which is opposite to the case observed in the II-VI DMS's. This has been already mentioned above in connection with Fig. 7.

For example, the σ^- and σ^+ transitions from the heavy-hole to conduction band are governed by the following combination (see Fig. 6) of the splittings in the valence and the conduction bands:

$$\Delta\left(j=\pm\frac{3}{2}\rightarrow j=\pm\frac{1}{2}\right)=\Delta_c\left(\pm\frac{1}{2}\right)-\Delta_v\left(\pm\frac{3}{2}\right)=\pm A_F x\langle S_z\rangle N_0(\alpha-\beta). \quad (9)$$

Thus the fundamental band edges for σ^- and σ^+ heavy-hole transitions are

$$\hbar\omega_{hh}^{\mp}=E_g+\Delta\left(j=\pm\frac{3}{2}\rightarrow j=\pm\frac{1}{2}\right)=E_g\pm A_F x\langle S_z\rangle N_0(\alpha-\beta). \quad (10)$$

These band edges replace E_g in Eq. (2)—i.e., $E_g\rightarrow\hbar\omega_{hh}^{\mp}$. It is straightforward from Fig. 6 to calculate the band edges for all the other transitions (LH, SO$\rightarrow D$). For each valence band the position of the Fermi level (E_F) has to be taken into account, which finally determines E_F in Eq. (2) for all contributing bands: for example (see Fig. 6),

TABLE I. Interband dielectric constant parameters for GaAs.

Gap energy E_g [eV]	Split-off energy (SO) Δ_0 [eV]	ε_∞	Oscillator strength f_{HH} [(eV)$^{3/2}$]
1.53	0.34	13	2.46

$$\hbar\omega_{F,hh}^{-} = E_F, \tag{11}$$

$$\hbar\omega_{F,lh}^{-} = (E_F - \Delta_{hh} + \Delta_{lh}). \tag{12}$$

Using Eqs. (11) and (12) and making the corresponding substitutions of E_F in Eq. (2) for all the possible transitions, the Moss-Burstein shift can then be explicitly taken into account. For all transitions, a damping term Γ_k is introduced by substituting $\omega \rightarrow \omega + i\Gamma_k$ according to Eq. (3). The resulting dielectric functions are found to be in good agreement with recently published ellipsometric data of Burch *et al.*[25] in the photon energy range 1.5–2.5 eV.

Optical constants $n^{\pm}$ were then derived from the dielectric functions following standard procedure, and we then used Fresnel's formulas and the thickness d of the GaMnAs layer to calculate the amplitude reflection coefficients $r^{\pm}$ for both circular polarizations:

$$r^{\pm}(\omega) = \frac{\rho_{01}^{\pm} + \rho_{12}^{\pm}\exp(2in^{\pm}\omega d/c_0)}{1 + \rho_{01}^{\pm}\rho_{12}^{\pm}\exp(2in^{\pm}\omega d/c_0)} = r_x(\omega) \pm ir_y(\omega). \tag{13}$$

The coefficients $\rho_{ij}^{\pm}$ are the half-space amplitude reflection coefficients between different media (subscripts $i,j=0$ for air, $=1$ for GaMnAs, $=2$ for GaAs substrate) according to Fresnel's formulas

$$\rho_{01}^{\pm} = \frac{n_{\mathrm{GaMnAs}}^{\pm} - n_{air}}{n_{\mathrm{GaMnAs}}^{\pm} + n_{air}}, \quad \rho_{12}^{\pm} = \frac{n_{\mathrm{GaAs}} - n_{\mathrm{GaMnAs}}^{\pm}}{n_{\mathrm{GaAs}} + n_{\mathrm{GaMnAs}}^{\pm}}. \tag{14}$$

In the derivations an explicit circular dispersion and dichroism are anticipated only for the thin magnetic GaMnAs layer, but not for the GaAs substrate (which is believed to exhibit negligible splitting). The Kerr rotation angle Θ (in degrees) is the inverse tangent of (r_y/r_x), [see the second part of Eq. (13)]:

$$\Theta = -\frac{180}{\pi}\arctan\left(\mathrm{Re}\left[i\frac{r^{+} - r^{-}}{r^{+} + r^{-}}\right]\right). \tag{15}$$

A quantity that is very convenient to measure is the reflectance MCD, because it is directly accessible in the experiment by simultaneously detecting the sum and difference of the power reflectances for both polarizations:

$$\mathrm{MCD}(\omega) = \frac{90}{\pi}\frac{r^{+\star}r^{+} - r^{-\star}r^{-}}{r^{+\star}r^{+} + r^{-\star}r^{-}} = \frac{90}{\pi}\frac{R^{+} - R^{-}}{R^{+} + R^{-}}. \tag{16}$$

In Table I the relevant parameters for simulating the Kerr rotation and MCD of the "test sample" $Ga_{1-x}Mn_xAs$ ($x=0.014$) are given. It should be noted that most of the parameters are required to closely resemble those of the host GaAs; particularly the energy gaps $E_g=1.50-1.57$ eV are very close to the gap of GaAs (1.53 eV).

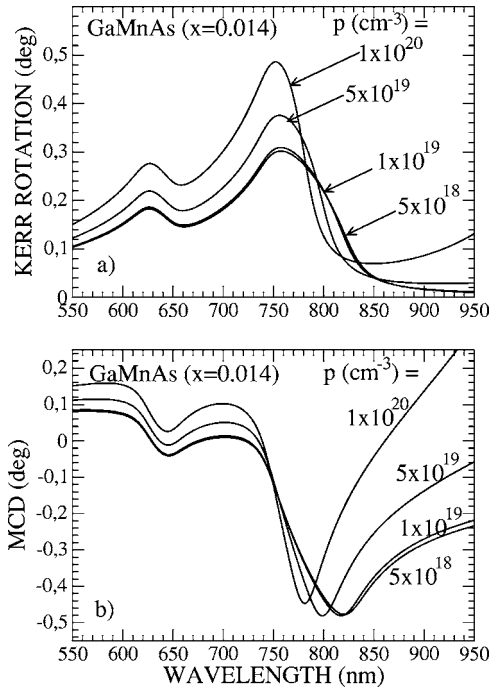

FIG. 8. Calculations of the Kerr rotation (a) and MCD signal (b) as a function of wavelength for the $Ga_{1-x}Mn_xAs$ sample with $x=0.014$. The different curves correspond to different hole concentrations p (cm^{-3}), showing the growing importance of the hole contribution as their concentration becomes large.

Figure 8 summarizes the results of the simulations for the reflectance Kerr rotation [Fig. 8(a)] and MCD [Fig. 8(b)] of a thin (300 nm) layer of GaMnAs ($x=0.014$) grown on a GaAs substrate. The sample is assumed to be exposed to a perpendicular saturating magnetic field. The hole concentration is the only variable parameter ($p=5\times10^{18}-1\times10^{20}$ cm^{-3}), and all other parameters are taken from Table I. In the short-wavelength region the most apparent dip comes from the onset of transitions originating from the split-off (SO) band ($\lambda<700$ nm). In the transparent regime ($\lambda>820$ nm) a residual Kerr effect comes from the free-carrier (hole) contribution, as is most clearly revealed for the $p=1\times10^{20}$ cm^{-3} plot in Fig. 8. The Moss-Burstein shift is clearly demonstrated in both figures: The strong drop-offs in the Kerr rotation and the MCD are both considerably shifted to shorter wavelengths with increasing hole concentrations at large values of p (larger than 10^{19} cm^{-3}).

IV. RESULTS AND DISCUSSION

A. Wavelength dependence of the magneto-optical Kerr effect and magnetic circular dichroism

In order to define a unique magnetic state we applied a sufficiently strong perpendicular magnetic field to saturate the GaMnAs samples ($x=0.014, x=0.03$) at low temperatures $T=1.8$ K—i.e., far below the Curie temperatures for either of the samples ($T_c=40$ K for $x=0.014$, $T_c=60$ K for

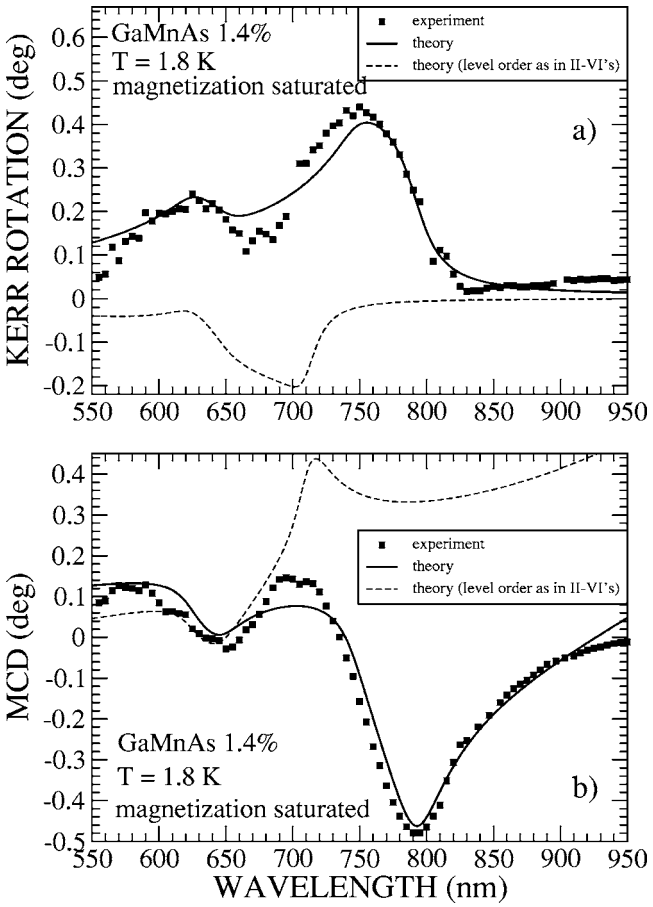

FIG. 9. Kerr rotation (a) and MCD signal (b) as a function of wavelength at $T=1.8$ K for the $Ga_{1-x}Mn_xAs$ sample with $x=0.014$, with magnetization saturated. Solid curve: calculation (parameters as in Table II). Squares: experimental data. Dashed curve: calculation with the same parameters but with level ordering as in the II-VI-based DMS's.

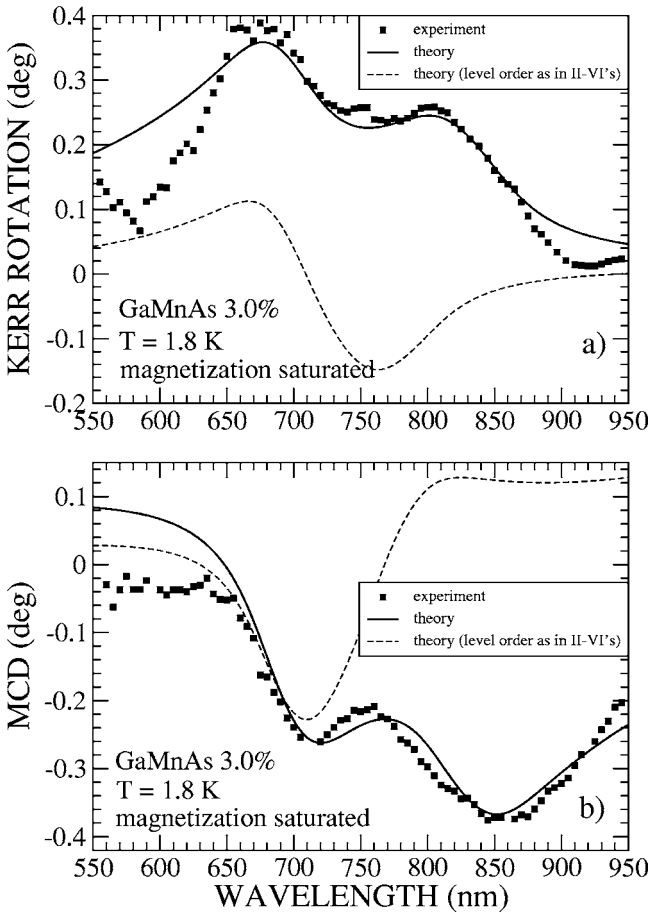

FIG. 10. Kerr rotation (a) and MCD signal (b) as a function of wavelength at $T=1.8$ K for the $Ga_{1-x}Mn_xAs$ sample with $x=0.03$, with magnetization saturated. Solid curve: calculation (parameters as in Table II). Squares: experimental data. Dashed curve: calculation with the same parameters but with level ordering as in the II-VI-based DMS's.

$x=0.03$). The wavelengths of the incoherent light source used in this experiment have been tuned from 550 nm to 950 nm, covering a rather wide spectral range in the absorption regime of the thin samples ($d=300$ nm). Figures 9 and 10 show the measured Kerr rotation data [Fig. 9(a), $x=0.014$; Fig. 10(a), $x=0.03$] and MCD [Fig. 9(b), $x=0.014$; Fig. 10(b), $x=0.03$] together with simulations, which show even quantitative agreement with the experimental results. As in Ref. 14, we recognize again the "stable" (negative) peak at $\lambda \approx 667$ nm (1.85 eV) and a peak at $\lambda = 767$ nm (1.61 eV), which varies strongly with hole concentration. Obviously the temperature dependence of the hole concentration modifies (shifts) this latter peak as quoted by Ref. 14, whereas the spectral position of the former peak ($\lambda \approx 667$ nm) does not at all depend on the hole concentration (see Fig. 8). The samples had sufficiently different manganese as well as hole concentrations (nominally $p=8.7 \times 10^{19}$ cm^{-3} for the $x=0.014$ sample and $p=7.6 \times 10^{18}$ cm^{-3} for $x=0.03$, as determined by room-temperature Hall effect measurements), thus providing the opportunity for testing the reliability of our dielectric function model over a rather wide range of sample parameters. It is important to note that Kerr rotation and MCD data were fitted together, resulting in one set of parameters for each sample. The most important aspect of the calculation was the choice of the exchange parameter $N_0\beta$, which had to be adjusted correspondingly for both samples in order to achieve agreement with the experiment. In particular, the sign of $N_0\beta$ had to be reversed from its antiferromagnetic character familiar from II-VI DMS's to ferromagnetic ($N_0\beta > 0$). If one would keep the sign of the conventional (II-VI) DMS exchange interaction parameter, an inevitable deviation of the calculated Kerr rotation and MCD from the experimental data would result (see the dashed lines in Figs. 9 and 10). Table II lists the relevant parameters (which were adjusted for the best fit). It is obvious that for the sample with lower manganese content ($x=0.014$) the damping factors Γ_k for transitions from HH and LH bands are lower than those for $x=0.03$.

The nominal dopant concentration as determined by Hall measurements (7.6×10^{18} cm^{-3}; see Sec. II A) is about 25% below the fitted $p=9.5 \times 10^{18}$ cm^{-3} for the sample with $x=0.03$ and is by a factor of ca. 1.3 larger for the sample with $x=0.014$, for which the best fit is obtained with $p=6.7$

TABLE II. Parameters used for fitting to experimental data in Fig. 9 (for $x=0.014$) and in Fig. 10 (for $x=0.03$).

Sample GaMnAs	Hole concentration p [10^{19} cm^{-3}]	Gap energy E_g [eV]	Split-off energy (SO) Δ_0 [eV]	Exchange energy (C) αN_0 [eV]	Exchange energy (HH) βN_0 [eV]	Mn-spin average $\langle S_Z \rangle$
$x=0.014$	6.7	1.57	0.37	0.22	+2.3	2.5
$x=0.03$	0.95	1.50	0.29	0.29	+0.90	2.5

Sample GaMnAs		Oscillator strength [(eV)$^{3/2}$]			Damping [meV]		
	ε_∞	f_{HH}	f_{LH}	f_{SO}	Γ_{HH}	Γ_{LH}	Γ_{SO}
$x=0.014$	18.6	8.5	0.4	6.8	30	20	40
$x=0.03$	11.8	5.4	0.7	12.2	75	40	85

$\times 10^{19}$ cm^{-3} as compared to $p=8.7\times 10^{19}$ cm^{-3} as determined by the Hall effect. Given that there is some uncertainty in the Hall data due to complications from the AHE, we find this comparison quite gratifying.

Here one needs to comment on this required modification of the carrier concentration: The experimental determination of the hole concentration from Hall measurements in ferromagnetic systems is ambiguous in the high doping regime ($p>1\times 10^{19}$ cm^{-3}) due to contributions from the AHE terms, allowing for considerable uncertainty in the value of this parameter. On the other hand, our extracted value of the Fermi level depends on the chosen band structure model for the interband dielectric function. We adopted in the valence band a parabolic energy-momentum dispersion for all participating bands and found that the most consistent fit is obtained by assertion of a dispersionless level in the conduction band (denoted as $|D\pm 1/2\rangle$ in Fig. 6). When we employ the rather strong (GaAs-like) conduction-band (CB) dispersion (shown as dashed lines in Fig. 6), the energy gap opens too rapidly to match the excitation from the highly depopulated valence band. A drastic reduction of the value of E_g in the fitting process (to the value of 1.2 eV) in order to achieve agreement with experiment seems us to be unphysical. However, if a dispersionless final state $|D\pm 1/2\rangle$ is assumed to lie near the band edge, we obtain $\hbar\omega_g=1.57$ eV and 1.50 eV for the energy gaps of $Ga_{1-x}Mn_xAs$ for $x=0.014$ and $x=0.03$, respectively—values that are reasonably close to that of GaAs (1.53 eV). In addition, the fairly good agreement with the nominal values of hole concentrations obtained from Hall measurements supports our model of the chosen transition levels. The existence of a rather high density-of-states level in the conduction band is also manifested by recent supercell and frozen-magnon calculations of the $Ga_{1-x}Mn_xAs$ band structure,[26] where a corresponding manganese-related peak is found in the Stoner-split (spin-down) conduction band just near the fundamental GaAs band edge (see Fig. 1, $x=0.031\ 25$ panel, of this Ref. 26).

The split-off energy Δ_0 had to be slightly modified with respect to the GaAs value of 0.34 eV (measured from the top of the valence band) to 0.37 eV for $x=0.014$ and to 0.29 eV for $x=0.03$, respectively. The exchange splitting $N_0\alpha$ keeps a comparable value for both samples (0.22–0.29 eV), but $N_0\beta$ differs significantly from the commonly accepted DMS picture, because the exchange interaction in ferromagnetic III-V DMS's is augmented by an additional interaction channel: Apart from the (i) local kinetic exchange which is antiferromagnetic, a second channel (ii) of a carrier-driven RKKY exchange is active which is oscillating with Mn—Mn distance, but predominantly ferromagnetic for coupled Mn spins on nearest sites and for hole concentrations $p<10^{20}$ cm^{-3}.[27] From Table II it is seen that $N_0\beta$ has its largest value (+2.3 eV) for the sample with $x=0.014$, which has the highest hole concentration. With the decrease of carrier concentration $N_0\beta$ is diminished correspondingly ($N_0\beta=+0.9$ eV; see Table II for $x=0.03$ and $p=9.5\times 10^{18}$ cm^{-3}). Linearly extrapolating the logarithmic scale of the concentration to $p=10^{17}$ cm^{-3} (nominally undoped GaMnAs), the kinetic antiferromagnetic exchange $N_0\beta=-2.36$ eV is restored, which is twice that of II-VI DMS's.

Since the magneto-optical effects depend on transitions from levels of different exchange splittings (and varying signs), the Kerr rotation and MCD must not necessarily scale with magnetization as measured by SQUID magnetometry. Indeed, the magnitudes of Kerr rotation for the $x=0.014$ and $x=0.03$ samples are of comparable size [Figs. 10(a) and 11(a)] in spite of a more than twofold increase of Mn concentration. Most stringent is the nonreversed sign of the spin-orbit spin-split level (SO), which appears not to be influenced by hybridization with the hole carriers, since the Fermi level is only degenerate with the HH and LH bands. Thus, the SO splitting keeps the sign as that of the II-VI DMS. Apart from such sign reversal the survival of the DMS approach is clearly manifested by the success of our fits to the Kerr rotation and MCD spectra. The role of strain in the $Ga_{1-x}Mn_xAs$ epilayers is not taken into account explicitly, but it is implicitly responsible for the distinct hysteresis splittings (Fig. 5) as a function of temperature, because the magnetocrystalline anisotropy is determined by strain, by the hole concentration, and by the temperature, as well as by the mutual spin-orbit coupling between the carriers, the lattice, and the magnetic moments of manganese ions.

B. Sign of $N_0\beta$

Although in most of the literature on GaMnAs an antiferromagnetic exchange interaction is assumed between the

valence-band holes and the Mn^{++} moments—as is the case for diluted magnetic II-VI DMS's—the sign of $N_0\beta$ has never been unambiguously established. In fact various authors have reported widely differing results for this parameter, varying in value and/or the sign over the range from +2.5 eV (ferromagnetic exchange) (Refs. 28–30) to −1.2 eV (antiferromagnetic exchange) (Refs. 11, 31, and 32). Our results strongly favor the ferromagnetic exchange interaction, resulting in a level order as plotted in Fig. 6—opposite to that observed in II-Mn-VI DMS's. There are several reasons for this order reversal.

(i) We observe the signs of the Kerr rotation in GaMnAs and CdMnTe to be different. This can either be caused by different signs of $N_0\beta$ or by a strong Moss-Burstein shift in the heavily doped GaMnAs, explicitly treated by Szczytko *et al.* for samples with $x>0.03$.[13] However, also *bulk* GaMnAs material with considerably lower Mn concentration (in which a sizable Moss-Burstein shift can certainly be neglected) exhibits a Faraday rotation opposite in sign from CdMnTe (see Fig. 7). This is in accordance with an earlier work of Szczytko *et al.*[28] for bulk GaMnAs ($x=0.000\,22$). Calculation of magneto-optic transitions in the parabolic band model indicates that a Moss-Burstein-induced change of level ordering occurs only for hole concentrations above $p=1\times10^{20}$ cm^{-3} (i.e., when the hole Fermi level $E_F>100$ meV). The Fermi energies of our samples are 76 meV (for $x=0.014$) and 21 meV (for $x=0.03$). Also from anomalous Hall effect measurements we estimate the carrier concentration of our samples to be below the threshold concentration for $E_F\approx100$ meV. We can therefore rule out the Moss-Burstein shift as the cause for the observed sign reversal.

(ii) The most striking evidence for the reversed level ordering in the valence band stems from the comparison of experimental data with model calculations in which both ferromagnetic and antiferromagnetic exchange in the valence band are plotted. The dashed lines in Figs. 9 and 10 are calculated with the level ordering according to antiferromagnetic (II-VI-DMS-like) exchange. Clearly there is in that case no agreement with the experimental data. In fact there does not exist any set of parameters (even drastic steps, such as a change of the fundamental energy gap) which can describe the experimental results correctly with antiferromagnetic level ordering. The solid lines calculated for ferromagnetic exchange, on the other hand, do show all the features present in the experimental data.

(iii) The main reason for the change of the exchange interaction in III-V-based dilute magnetic semiconductors is the alteration of the kinetic exchange between the Mn acceptor and the hole carrier states. In GaMnAs the trivalent bond of Ga is replaced by the divalent Mn^{++}, which becomes a d^4 level to maintain neutrality. This magnetic impurity attracts an (eventually tightly bound) electron from the valence band, thus forming the stable d^5 half-filled shell of Mn and releasing a hole in the valence band. Such an A^- center by itself can capture the loosely bound hole (thus forming an A^0 center). The interplay and balance between A^- and A^0 centers controls the on-site exchange interaction to be either ferromagnetic ($N_0\beta>0$) for A^0 or antiferromagnetic ($N_0\beta<0$) for A^-. One must infer that the A^0 centers prevail in our samples—a reasonable assumption when the hole concentration is sufficiently low to avoid ionization of the loosely bound holes due to screening of the Coulomb interaction.

Finally we comment on the consistency of our fitted hole-manganese exchange parameter $N_0\beta$ with calculations of the Curie temperature in the mean-field and virtual-crystal approximation, as outlined recently by Brey and Gomez-Santos:[27]

$$k_BT_C = 1/(3\mu_0)S^2(J_{pd}/g\mu_B)^2\chi_P x N_0 \approx 1.38\times10^7\chi_P\ [\mathrm{K}]. \tag{17}$$

From Eq. (17) it can be seen that only the modulus of the exchange parameter J_{pd} (but not its sign) can be derived from a measurement of the Curie temperature T_C. The numerical value obtained in Eq. (17) is valid for $|J_{pd}|=\beta=0.1035$ eV nm^3 (according to $N_0\beta=2.3$ eV), $x=0.014$, and $N_0=2.21\times10^{22}$ cm^{-3}. χ_P denotes the Pauli spin susceptibility of the holes (HH-hole spin moment jP_s with $j=3/2$ and spin polarization P_s), which can be expressed in the degenerate case (large carrier concentration $p=6.7\times10^{19}$ cm^{-3}, $E_F=76$ meV) as

$$\chi_P = \mu_0 g^2\mu_B^2 j(j+1)P_s^2(3/2)p/E_F \approx 1.34\times10^{-5}P_s^2 \quad \text{for } p=6.7\times10^{19}\ \mathrm{cm}^{-3}. \tag{18}$$

Combining both Eqs. (17) and (18) one obtains for $T_C\approx40$ K a spin polarization $P_s=0.46$. This reasonable estimate in turn justifies the mean-field and virtual-crystal approximation, which has been taken as the basis for our theoretical DMS model.

Finally, the order of the oscillator strength for the HH $\rightarrow$CB transitions has to be revisited, since the terminating interband transition level in the conduction band is dispersionless. An analytic expression for the oscillator strength in the parabolic band model is

$$f = \frac{e^2\mu^{3/2}}{2\pi\varepsilon_0 m_0^2\hbar}|\langle \mathrm{CB}|p|\mathrm{HH}\rangle|^2, \tag{19}$$

where $|\langle \mathrm{CB}|p|\mathrm{HH}\rangle|^2$ is the dipole matrix element and $\mu=0.0695m_0$ denotes the reduced density-of-states (DOS) mass derived from the CB and HH band-edge masses $\mu_{CB}=0.08m_0$ and $\mu_{HH}=0.53m_0$, respectively. In the case of a dispersionless CB level we replace μ_{CB} by $\mu_{CB}=\infty$, which gives $\mu=\mu_{HH}=0.53m_0$, considerably larger than the value $\mu=0.0695m_0$ obtained for a dispersive conduction band. Thus the oscillator strength is expected to be considerably higher in the present case than for GaAs ($f=2.46$ eV$^{3/2}$). Our fits ($f=8.5$ eV$^{3/2}$) to the magneto-optical spectra confirm an increase of the density-of-states mass from $\mu=0.0695m_0$ to $\mu=0.16m_0$ which corresponds to 30% of the heavy-hole mass.

V. CONCLUSION

Magneto-optical Kerr rotation and magnetic circular dichroism have been used as tools for investigating thin layers of the ferromagnetic semiconductor GaMnAs on GaAs substrates. We used two samples in this investigation that were sufficiently diverse with respect to their Curie temperatures

and the orientations of their easy axes of magnetization, as well as the concentrations of both magnetic ions and holes, to experimentally demonstrate the versatility of our analytic model for the interband dielectric function, which explicitly takes into account the Moss-Burstein shift. The model is convenient, in that it allows for a simultaneous calculation of the wavelength-dependent Kerr rotation and Kerr ellipticity for various hole concentrations. The excellent agreement between magneto-optical and SQUID magnetization data at temperatures far below the Curie temperature provides strong support that the mean-field exchange interaction model adopted from II-VI-based diluted magnetic semiconductors provides a correct description for the problem at hand. However, the model indicates that the angular momentum level sequence in the depopulated spin-split valence band is reversed with respect to the II-VI-based DMS's. Furthermore, deviations of the temperature dependences of saturation magnetization from the mean-field behavior indicate the presence of a strong correlation between the free holes and the manganese spins. The six-band Luttinger-Kohn $(\vec{k}\cdot\vec{p})$-band model is sufficiently accurate to reconcile theory with experiment without the need to invoke extensive computational efforts and without requiring significant departure in values of band parameters from those of the parent GaAs, particularly of oscillator strengths and energy gaps. This latter claim (to keep the energy gap near the GaAs value) could, however, only be satisfied by assuming that the transitions determining the magneto-optical effects of interest involve a dispersion-less level in the conduction band regime instead of a GaAs-like parabolic band dispersion. Recent theoretical works predict such a level mediated by exchange interaction of spin-polarized electrons with manganese ions.

In the magneto-optical experiments described herein a saturating magnetic field was applied perpendicular to the film plane, in order to obtain the highest possible values of the Kerr effect due to the polar geometry. The values of the exchange splitting parameters $N_0\alpha=0.22-0.29$ eV and $N_0\beta$ adjusted to +2.3 eV (for $x=0.014$, $p=6.7\times10^{19}$ cm^{-3}) and +0.9 eV (for $x=0.03$, $p=9.5\times10^{18}$ cm^{-3}), respectively, further serve to substantiate the validity of the DMS mean-field picture.

In summary, the model presented here is not intended to provide a complete description of linear magneto-optical effects in ferromagnetic III-V-based semiconductors (e.g., it does not take into account band structure properties beyond the parabolic limit), but we have demonstrated it to be a manageable tool for simulating the polar Kerr and magnetic circular dichroism spectra over a rather wide range of photon frequencies not only qualitatively, but with reasonable quantitative accuracy.

ACKNOWLEDGMENTS

We thank Professor A. K. Ramdas for giving the bulk GaMnAs sample to our disposal. Financial support of DFG, Bonn (International Research Training Group "Non-Equilibrium Phenomena and Phase Transitions in Complex Systems") and of the Österreich. Fonds zur Frderung der wissenschaftlichen Forschung, under Project No. P 15397 is gratefully acknowledged. The Notre Dame part of the work was supported by National Science Foundation Grant Nos. DMR02-10519 and DMR02-45227.

APPENDIX: DERIVATION OF THE INTERBAND DIELECTRIC FUNCTION FOR PARABOLIC ENERGY BANDS IN THE PRESENCE OF A HIGH CARRIER CONCENTRATION

From Adachi (see Ref. 24) we adopt the formula for the absorptive part of the interband dielectric function:

$$\varepsilon_2(\omega)=\frac{f}{(\hbar\omega)^2}\sqrt{\hbar\omega-E_g}\quad(\hbar\omega>E_g). \tag{A1}$$

The electric-dipole oscillator strength f depends primarily on the $\frac{3}{2}$ power of the joint-density-of-states mass—i.e., the reduced mass between the conduction- and valence-band effective masses ($m_c/m_0=0.067$, $m_{HH}/m_0=0.5$, $m_{LH}/m_0=0.086$ for GaAs). The most relevant dependence is the square root of the photon frequency ω, which must exceed the energy gap E_g for interband transitions. Formula (A1) is correct for sharp energy band states and an empty conduction band.

In the case of a filled band the interband transition starts at a larger energy than the energy gap:

$$\hbar\omega>E_g+E_F. \tag{A2}$$

The Fermi energy (E_F) is either the population level of electrons in the conduction band or the depopulation level (i.e., the population level of holes) in the valence band. In this special case of unbroadened band levels the KK transformation can be performed analytically to obtain the dispersive part (ε_1) of the dielectric function. We find [using $\varepsilon_2(-\omega)=-\varepsilon_2(\omega)$] that

$$\begin{aligned}\varepsilon_1(\omega)-\varepsilon_\infty&=\frac{1}{\pi}P\int_{-\infty}^{+\infty}\frac{\varepsilon_2(\omega')}{\omega'-\omega}d\omega'\\&=\frac{1}{\pi}\int_{\omega_g+\omega_F}^{\infty}\frac{\varepsilon_2(\omega')}{\omega'+\omega}d\omega'+\frac{1}{\pi}\int_{\omega_g+\omega_F}^{\infty}\frac{\varepsilon_2(\omega')}{\omega'-\omega}d\omega.\end{aligned} \tag{A3}$$

Since the absorption ε_2 below E_g+E_F is zero, we have replaced the lower limit of integration (=0) in the last expression of Eq. (A3) by E_g+E_F. After a lengthy calculation (using the substitution $\sqrt{\hbar\omega-E_g}=x$ and partial fraction decomposition), the following expression for the dispersive part of the interband dielectric function is obtained:

$$\varepsilon_1(\omega)-\varepsilon_\infty = 2f\frac{\sqrt{E_g}}{(\hbar\omega)^2}\left[1-\frac{2}{\pi}\arctan\sqrt{\frac{E_F}{E_g}}\right] - f\frac{\sqrt{E_g}}{(\hbar\omega)^2}\sqrt{1+\frac{\hbar\omega}{E_g}}\left[1-\frac{2}{\pi}\arctan\sqrt{\frac{E_F}{E_g+\hbar\omega}}\right] - f\frac{\sqrt{E_g}}{(\hbar\omega)^2}\sqrt{1-\frac{\hbar\omega}{E_g}}\left[1-\frac{2}{\pi}\arctan\sqrt{\frac{E_F}{E_g-\hbar\omega}}\right]. \quad \text{(A4)}$$

For the case of empty bands ($E_F=0$) we retain the formula given by Adachi (see Ref. 24):

$$\varepsilon_1(\omega)-\varepsilon_\infty = f\frac{\sqrt{E_g}}{(\hbar\omega)^2}\left(2-\sqrt{1+\frac{\hbar\omega}{E_g}}-\sqrt{1-\frac{\hbar\omega}{E_g}}\right). \quad \text{(A5)}$$

*Corresponding author.

[1] H. Ohno, A. Shen, F. Matsukura, A. Oiwa, A. Endo, and S. Kutsumotu, Appl. Phys. Lett. **69**, 363 (1996).

[2] M. Tanaka and Y. Higo, Phys. Rev. Lett. **87**, 026602 (2001).

[3] T. Shono, T. Hasegawa, and T. Fukumura, Appl. Phys. Lett. **77**, 1363 (2000).

[4] T. Dietl, J. König, and A. MacDonald, cond-mat/0107009 (unpublished).

[5] D. Hrabovsky, E. Vanella, A. Fert, D. Yee, J. Redoules, J. Sadowski, J. Kanski, and L. Ilver, Appl. Phys. Lett. **81**, 2806 (2002).

[6] H. Shimizu and M. Tanaka, J. Appl. Phys. **91**, 7287 (2002).

[7] A. Oiwa, T. Slubinski, and H. Munekata, Appl. Phys. Lett. **78**, 518 (2001).

[8] A. V. Kimel, G. V. Astakhov, G. M. Schott, A. Kirilyuk, D. R. Yakovlev, G. Karczewski, W. Ossau, G. Schmidt, L. W. Molenkamp, and T. Rasing, Phys. Rev. Lett. **92**, 237203 (2004).

[9] G. P. Moore, J. Ferre, A. Mougin, M. Moreno, and L. Däweritz, J. Appl. Phys. **94**, 4530 (2003).

[10] M. Abolfath, T. Jungwirth, J. Brum, and A. H. MacDonald, Phys. Rev. B **63**, 054418 (2001).

[11] T. Dietl, H. Ohno, and F. Matsukura, Phys. Rev. B **63**, 195205 (2001).

[12] M. Sawicki, F. Matsukura, T. Dietl, G. Schott, C. Ruester, G. Schmidt, L. Molenkamp, and G. Karczewski, J. Supercond. **16**, 7 (2003).

[13] J. Szczytko, W. Mac, A. Twardowski, F. Matsukura, and H. Ohno, Phys. Rev. B **59**, 12935 (1999).

[14] B. Beschoten, P. A. Crowell, I. Malajovich, D. D. Awschalom, F. Matsukura, A. Shen, and H. Ohno, Phys. Rev. Lett. **83**, 3073 (1999).

[15] H. Ohno, H. Munekata, T. Penney, S. von Molnar, and L. L. Chang, Phys. Rev. Lett. **68**, 2664 (1992).

[16] A. Oiwa, S. Katsumoto, A. Endo, M. Hirasawa, Y. Iye, F. Matsukura, A. Shen, Y. Sugawara, and H. Ohno, Physica B **249–251**, 775 (1998).

[17] X. Liu, Ph.D. thesis, University of Notre Dame, 2002.

[18] H. Ohno, J. Magn. Magn. Mater. **200**, 110 (1999).

[19] G. M. Schott, W. Faschinger, and L. W. Molenkamp, Appl. Phys. Lett. **79**, 1807 (2001).

[20] D. Ruzmetov, J. Scherschligt, D. V. Baxter, T. Wojtowicz, X. Liu, Y. Sasaki, J. K. Furdyna, K. M. Yu, and W. Walukiewicz, Phys. Rev. B **69**, 155207 (2004).

[21] X. Liu, Y. Sasaki, and J. K. Furdyna, Phys. Rev. B **67**, 205204 (2003).

[22] S. Das Sarma, E. H. Hwang, and A. Kaminski, Phys. Rev. B **67**, 155201 (2003).

[23] M. Sawicki, in *Proceedings of the 2nd International Conference on Physics and Applications of Spin Related Phenomena in Semiconductors*, edited by L. W. Molenkamp (IOP, Wrzburg, 2002).

[24] S. Adachi, *Physical Properties of III-V Semiconductor Compounds: InP, InAs, GaAs, GaP, InGaAs and InGaAsP* (Wiley-Interscience, New York, 1992).

[25] K. S. Burch, J. Stephens, R. K. Kawakami, D. D. Awschalom, and D. N. Basov, Phys. Rev. B **70**, 205208 (2004).

[26] L. M. Sandratskii and P. Bruno, Phys. Rev. B **66**, 134435 (2002).

[27] L. Brey and G. Gomez-Santos, Phys. Rev. B **68**, 115206 (2003).

[28] J. Szczytko, W. Mac, A. Stachow, A. Twardowski, P. Becla, and J. Tworzydlo, Solid State Commun. **99**, 927 (1996).

[29] A. Twardowski, Mater. Sci. Eng., B **63**, 96 (1999).

[30] T. Hartmann, M. Lampalzer, W. Stolz, K. Megges, J. Lorberth, P. Klar, and W. Heimbrodt, Thin Solid Films **364**, 209 (2000).

[31] J. Okabayashi, A. Kimura, O. Rader, T. Mizokawa, A. Fujimori, T. Hayashi, and M. Tanaka, Phys. Rev. B **58**, R4211 (1998).

[32] J. Szczytko, W. Bardyszewski, and A. Twardowski, Phys. Rev. B **64**, 075306 (2001).